

Order of Magnitude Smaller Limit on the Electric Dipole Moment of the Electron

The ACME Collaboration,* J. Baron,¹ W. C. Campbell,² D. DeMille,³† J. M. Doyle,¹† G. Gabrielse,¹† Y. V. Gurevich,¹‡ P. W. Hess,¹ N. R. Hutzler,¹ E. Kirilov,³§ I. Kozyryev,³|| B. R. O'Leary,³ C. D. Panda,¹ M. F. Parsons,¹ E. S. Petrik,¹ B. Spaun,¹ A. C. Vutha,⁴ A. D. West³

The Standard Model of particle physics is known to be incomplete. Extensions to the Standard Model, such as weak-scale supersymmetry, posit the existence of new particles and interactions that are asymmetric under time reversal (T) and nearly always predict a small yet potentially measurable electron electric dipole moment (EDM), d_e , in the range of 10^{-27} to 10^{-30} $e \cdot \text{cm}$. The EDM is an asymmetric charge distribution along the electron spin (\vec{S}) that is also asymmetric under T. Using the polar molecule thorium monoxide, we measured $d_e = (-2.1 \pm 3.7_{\text{stat}} \pm 2.5_{\text{sys}}) \times 10^{-29}$ $e \cdot \text{cm}$. This corresponds to an upper limit of $|d_e| < 8.7 \times 10^{-29}$ $e \cdot \text{cm}$ with 90% confidence, an order of magnitude improvement in sensitivity relative to the previous best limit. Our result constrains T-violating physics at the TeV energy scale.

The exceptionally high internal effective electric field \mathcal{E}_{eff} of heavy neutral atoms and molecules can be used to precisely probe for the electron electric dipole moment (EDM), d_e , via the energy shift $U = -\vec{d}_e \cdot \vec{\mathcal{E}}_{\text{eff}}$, where $\vec{d}_e = d_e \vec{S} / (\hbar/2)$, \vec{S} is electron spin, and \hbar is the reduced Planck constant. Valence electrons travel relativistically near the heavy nucleus, making \mathcal{E}_{eff} up to a million times the size of any static laboratory field (1–3). The previous best limits on d_e came from experiments with thallium (Tl) atoms (4) ($|d_e| < 1.6 \times 10^{-27}$ $e \cdot \text{cm}$) and ytterbium fluoride (YbF) molecules (5, 6) ($|d_e| < 1.06 \times 10^{-27}$ $e \cdot \text{cm}$). The latter demonstrated that molecules can be used to suppress the motional electric fields and geometric phases that limited the Tl measurement (5) [this suppression is also present

in certain atoms (7)]. Insofar as polar molecules can be fully polarized in laboratory-scale electric fields, \mathcal{E}_{eff} can be much greater than in atoms. The $H^3\Delta_1$ electronic state in the thorium monoxide (ThO) molecule provides an $\mathcal{E}_{\text{eff}} \approx 84$ GV/cm, larger than those previously used in EDM measurements (8, 9). This state's unusually small magnetic moment reduces its sensitivity to spurious magnetic fields (10, 11). Improved systematic error rejection is possible because internal state selection allows the reversal of \mathcal{E}_{eff} with no change in the laboratory electric field (12, 13).

To measure d_e , we perform a spin precession measurement (10, 14, 15) on pulses of $^{232}\text{Th}^{16}\text{O}$ molecules from a cryogenic buffer gas beam source that generate a laboratory electric field $\mathcal{E}_{\hat{z}}$ (Fig.

1A). A coherent superposition of two spin states, corresponding to a spin aligned in the xy plane, is prepared using optical pumping and state preparation lasers. Parallel electric ($\vec{\mathcal{E}}$) and magnetic (\vec{B}) fields exert torques on the electric and magnetic dipole moments, causing the spin vector to precess in the xy plane. The precession angle is measured with a readout laser and fluorescence detection. A change in this angle as $\vec{\mathcal{E}}_{\text{eff}}$ is reversed is proportional to d_e .

In more detail, a laser beam (wavelength 943 nm) optically pumps molecules from the ground electronic state into the lowest rotational level, $J = 1$, of the metastable (lifetime ~ 2 ms) electronic $H^3\Delta_1$ state manifold (Fig. 1B), in an incoherent mixture of the $\tilde{N} = \pm 1, M = \pm 1$ states. M is the angular momentum projection along the \hat{z} axis. \tilde{N} refers to the internuclear axis, \hat{n}_i , aligned (+1) or antialigned (–1) with respect to $\vec{\mathcal{E}}$, when $|\vec{\mathcal{E}}| \geq 1$ V/cm (11). The linearly polarized state preparation laser's frequency is resonant with the $H \rightarrow C$ transition at 1090 nm (Fig. 1B). Within the short-lived (500 ns) electronic C state, there are two opposite-parity $\tilde{P} = \pm 1$ states with $J = 1, M = 0$. For a given spin precession measurement, the laser frequency determines the \tilde{N} and \tilde{P} states that are addressed. This laser optically pumps the bright

¹Department of Physics, Harvard University, Cambridge, MA 02138, USA. ²Department of Physics and Astronomy, University of California, Los Angeles, CA 90095, USA. ³Department of Physics, Yale University, New Haven, CT 06511, USA. ⁴Department of Physics and Astronomy, York University, Toronto, Ontario M3J 1P3, Canada.

*The collaboration consists of all listed authors. There are no additional collaborators.

†Corresponding author. E-mail: acme@physics.harvard.edu (D.D., J.M.D., G.G.)

‡Present address: Department of Physics, Yale University, New Haven, CT 06511, USA.

§Present address: Institut für Experimentalphysik, Universität Innsbruck, A-6020 Innsbruck, Austria.

||Present address: Department of Physics, Harvard University, Cambridge, MA 02138, USA.

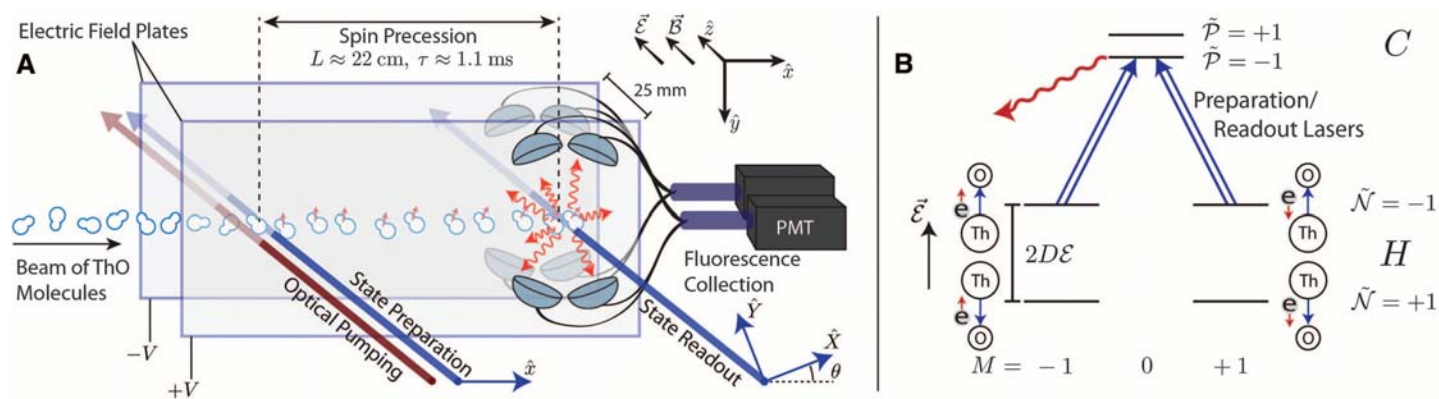


Fig. 1. Schematic of the apparatus and energy level diagram. (A) A collimated pulse of ThO molecules enters a magnetically shielded region (not to scale). An aligned spin state (smallest red arrows), prepared via optical pumping, precesses in parallel electric and magnetic fields. The final spin alignment is read out by a laser with rapidly alternating linear polarizations, \hat{X} and \hat{Y} , with the resulting fluorescence collected and detected with photomultiplier tubes (PMTs). (B) The state preparation and readout lasers (double-lined

blue arrows) drive one molecule orientation $\tilde{N} = \pm 1$ (split by $2D\mathcal{E} \sim 100$ MHz, where D is the electric dipole moment of the H state) in the H state to C , with parity $\tilde{P} = \pm 1$ (split by 50 MHz). Population in the C state decays via spontaneous emission, and we detect the resulting fluorescence (red wiggly arrow). H state levels are accompanied by cartoons displaying the orientation of $\vec{\mathcal{E}}_{\text{eff}}$ (blue arrows) and the spin of the electron (red arrows) that dominantly contributes to the d_e shift.

superposition of the two resonant $M = \pm 1$ sub-levels out of the H state, leaving behind the orthogonal dark superposition that cannot absorb the laser light; we use this dark state as our initial state (19). If the state preparation laser is polarized along \hat{x} , then the prepared state, $|\psi(\tau = 0), \tilde{N}\rangle$, has the electron spin aligned along the \hat{y} axis. The spin then precesses in the xy plane by angle ϕ to

$$|\psi(\tau), \tilde{N}\rangle = \frac{\exp(-i\phi)|M = +1, \tilde{N}\rangle - \exp(+i\phi)|M = -1, \tilde{N}\rangle}{\sqrt{2}} \quad (1)$$

Because $\vec{\mathcal{E}}$ and $\vec{\mathcal{B}}$ are aligned along \hat{z} , the phase ϕ is determined by $|\mathcal{B}_z| = |\vec{\mathcal{B}} \cdot \hat{z}|$, its sign, $\tilde{\mathcal{B}} = \text{sgn}(\vec{\mathcal{B}} \cdot \hat{z})$, and the electron's EDM, d_e :

$$\phi \approx \frac{-(\mu_B g \tilde{\mathcal{B}} |\mathcal{B}_z| + \tilde{N} \tilde{\mathcal{E}} d_e \mathcal{E}_{\text{eff}}) \tau}{\hbar} \quad (2)$$

where $\tilde{\mathcal{E}} \equiv \text{sgn}(\vec{\mathcal{E}} \cdot \hat{z})$, τ is the spin precession time, and $\mu_B g$ is the magnetic moment (15) of the $H, J = 1$ state where $g = -0.0044 \pm 0.0001$ is the gyromagnetic ratio and μ_B is the Bohr magneton. The sign of the EDM term, $\tilde{N} \tilde{\mathcal{E}}$, arises from the relative orientation between $\vec{\mathcal{E}}_{\text{eff}}$ and the electron spin, as illustrated in Fig. 1B.

After the spin precesses as each molecule travels over a distance of $L \approx 22$ cm ($\tau \approx 1.1$ ms), we measure ϕ by optically pumping on the same $H \rightarrow C$ transition with the state readout laser. The laser polarization alternates between \hat{X} and \hat{Y} every 5 μs , and we record the modulated fluorescence signals S_X and S_Y from the decay of C to the ground state (fig. S1A). This procedure amounts to a projective measurement of the spin onto \hat{X} and \hat{Y} , which are defined such that \hat{X} is at an angle θ with respect to \hat{x} in the xy plane (Fig. 1A). To cancel the effects of fluctuations in molecule number, we normalize the spin precession signal by computing the asymmetry

$$\mathcal{A} \equiv \frac{S_X - S_Y}{S_X + S_Y} = C \cos[2(\phi - \theta)] \quad (3)$$

(10), where the contrast C is $94 \pm 2\%$ on average. We set $|\mathcal{B}_z|$ and θ such that $\phi - \theta \approx (\pi/4)(2n + 1)$ for integer n , so that the asymmetry is linearly proportional to small changes in ϕ and is maximally sensitive to the EDM. We measure

C by dithering θ between two nearby values that differ by 0.1 rad, denoted by $\theta = \pm 1$.

We perform this spin precession measurement repeatedly under varying experimental conditions to (i) distinguish the EDM energy shift from background phases and (ii) search for and monitor possible systematic errors. Within a “block” of data (fig. S1C) taken over 40 s, we perform measurements of the phase for each experimental state derived from four binary switches, listed from fastest (0.5 s) to slowest (20 s): the molecule alignment- \tilde{N} , the \mathcal{E} -field direction $\tilde{\mathcal{E}}$, the readout laser polarization dither state $\tilde{\theta}$, and the \mathcal{B} -field direction $\tilde{\mathcal{B}}$. For each $(\tilde{N}, \tilde{\mathcal{E}}, \tilde{\mathcal{B}})$ state of the experiment, we measure \mathcal{A} and \mathcal{C} , from which we can extract ϕ . Within each block, we form “switch parity components” of the phase, ϕ^u , which are combinations of the measured phases that are odd or even under these switch operations (13). We denote the switch parity of a quantity with a superscript, u , listing the switch labels under which the quantity is odd; it is even under all unlabeled switches. For example, the EDM contributes to a phase component $\phi^{\tilde{N}\tilde{\mathcal{E}}} = -d_e \mathcal{E}_{\text{eff}} \tau / \hbar$. We extract the mean precession time τ from $\phi^{\tilde{\mathcal{B}}} = -\mu_B g |\mathcal{B}_z| \tau / \hbar$ and compute the frequencies, $\omega^u \equiv \phi^u / \tau$. The EDM value is obtained from $\omega^{\tilde{N}\tilde{\mathcal{E}}}$ by $d_e = -\hbar \omega^{\tilde{N}\tilde{\mathcal{E}}} / \mathcal{E}_{\text{eff}}$.

On a slower time scale, we perform additional “superblock” binary switches (fig. S1D) to suppress some known systematic errors and to search for unknown ones. These switches, which occur on time scales of 40 to 600 s, are the excited-state parity addressed by the state readout lasers, $\tilde{\mathcal{P}}$; a rotation of the readout polarization basis by $\theta \rightarrow \theta + \pi/2$, $\tilde{\mathcal{R}}$; a reversal of the leads that supply the electric fields, $\tilde{\mathcal{L}}$; and a global polarization rotation of both the state preparation and readout laser polarizations, $\tilde{\mathcal{G}}$. The $\tilde{\mathcal{P}}$ and $\tilde{\mathcal{R}}$ switches interchange the role of the \hat{X} and \hat{Y} readout beams and hence reject systematic errors associated with small differences in power, shape, or pointing. The two $\tilde{\mathcal{G}}$ state angles are chosen to suppress systematics that couple to unwanted ellipticity imprinted on the polarizations by birefringence in the electric field plates. The $\tilde{\mathcal{L}}$ switch rejects systematics that couple to an offset voltage in the electric field power supplies. We extract the EDM from $\omega^{\tilde{N}\tilde{\mathcal{E}}}$ after a complete

set of the 2^8 block and superblock states. The value of $\omega^{\tilde{N}\tilde{\mathcal{E}}}$ is even under all of the superblock switches.

The total data set consists of $\sim 10^4$ blocks of data taken over the course of ~ 2 weeks (fig. S1, E and F). During data collection, we also varied, from fastest (hours) to slowest (a few days), the \mathcal{B} -field magnitude, $|\mathcal{B}_z| \approx 1, 19, \text{ or } 38$ mG (corresponding to $|\phi| \approx 0, \pi/4, \text{ or } \pi/2$, respectively); the \mathcal{E} -field magnitude, $|\mathcal{E}_z| \approx 36$ or 141 V/cm; and the pointing direction of the lasers, $\hat{k} \cdot \hat{z} = \pm 1$. Figure 2B shows measured EDM values obtained when the data set is grouped according to the states of $|\mathcal{B}_z|$, $|\mathcal{E}_z|$, $\hat{k} \cdot \hat{z}$, and each superblock switch. All of these measurements are consistent within 2σ .

We computed the 1σ standard error in the mean and used standard Gaussian error propagation to obtain the reported statistical uncertainty. The reported upper limit was computed using the Feldman-Cousins prescription (20) applied to a folded normal distribution. To prevent experimental bias, we performed a blind analysis by adding an unknown offset to $\omega^{\tilde{N}\tilde{\mathcal{E}}}$. The mean, statistical error, systematic shifts, and procedure for calculating the systematic error were determined before unblinding. Figure 2A shows a histogram of EDM measurements. The asymmetry \mathcal{A} obeys a ratio distribution, which has large non-Gaussian tails in the limit of low signal-to-noise ratio (21). We applied a photon count rate threshold cut so that we included only data with a large signal-to-noise ratio, resulting in a statistical distribution that closely approximates a Gaussian. When the EDM measurements are fit to a constant value, the reduced χ^2 is 0.996 ± 0.006 . On the basis of the total number of detected photoelectrons (~ 1000 per pulse) that contributed to the measurement, the statistical uncertainty is 1.15 times that from shot noise (15).

To search for possible sources of systematic error, we varied more than 40 separate parameters (table S1) and observed their effects on $\omega^{\tilde{N}\tilde{\mathcal{E}}}$ and many other components of the phase correlated with \tilde{N} , $\tilde{\mathcal{E}}$, or $\tilde{\mathcal{B}}$. These parameters were intentionally applied tunable imperfections, such as transverse magnetic fields or laser detunings. These systematic checks were performed concurrently with the 8 block and superblock switches.

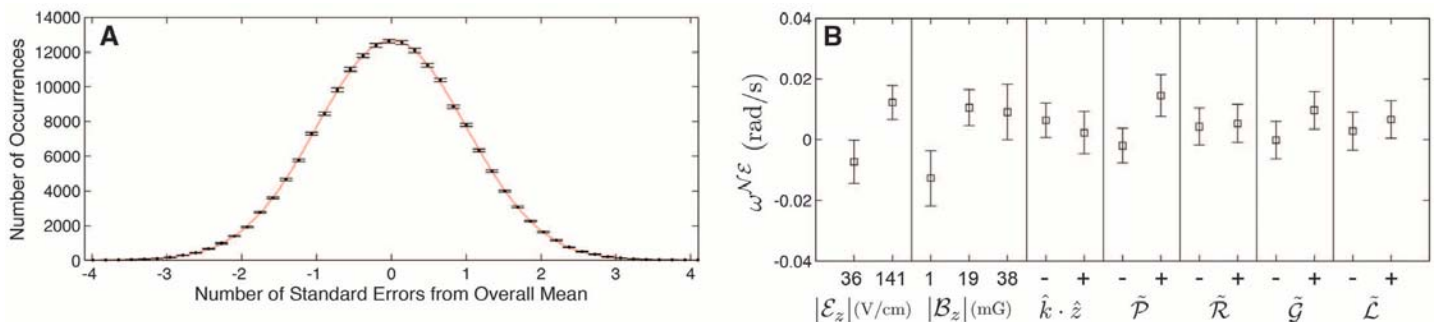


Fig. 2. Statistical spread of $\omega^{\tilde{N}\tilde{\mathcal{E}}}$ measurements. (A) Histogram of $\omega^{\tilde{N}\tilde{\mathcal{E}}}$ measurements for each time point (within the molecule pulse) and for all blocks. Error bars represent expected Poissonian fluctuations in each histogram bin. (B) Measured $\omega^{\tilde{N}\tilde{\mathcal{E}}}$ values grouped by the states of $|\mathcal{B}_z|$, $|\mathcal{E}_z|$, $\hat{k} \cdot \hat{z}$, and each superblock switch, before systematic corrections, with 1σ statistical error bars.

We assume that $\omega^{N\mathcal{E}}$ depends linearly on each parameter P , so that the possible systematic shift and uncertainty of $\omega^{N\mathcal{E}}$ is evaluated from the measured slope, $S = \partial\omega^{N\mathcal{E}}/\partial P$, and the parameter value during normal operation (obtained from auxiliary measurements). If S is not monitored throughout the data set, we do not apply a systematic correction but simply include the measured upper limit in our systematic error budget. Data taken with intentionally applied parameter imperfections are used only for determination of systematic shifts and uncertainties. Table 1 lists all contributions to our systematic error.

We identified two parameters that systematically shift the value of $\omega^{N\mathcal{E}}$ within our experimental resolution. Both parameters couple to the ac Stark shift induced by the lasers. The molecules are initially prepared in the dark state with a spin orientation dependent on the laser polarization. If there is a polarization gradient along the molecular beam propagation direction, the molecules acquire a small bright-state amplitude.

Away from the center of a Gaussian laser profile, the laser can be weak enough that the bright-state amplitude is not rapidly pumped away; it acquires a phase relative to the dark state due to the energy splitting between the bright and dark states, given by the ac Stark shift. An equivalent phase is acquired in the state readout laser. This effect changes the measured phase by $\phi_{ac}(\Delta, \Omega_r) \approx (\alpha\Delta + \beta\Omega_r)$, where Δ and Ω_r are the detuning from the $H \rightarrow C$ transition and the transition's Rabi frequency, respectively. The constants α and β are measured directly by varying Δ and Ω_r , and their values depend on the laser's spatial intensity and polarization profile. These measurements are in good agreement with our analytical and numerical models.

A large (~10%) circular polarization gradient is caused by laser-induced thermal stress birefringence (22) in the electric field plates. The laser beams are elongated perpendicular to the molecular beam axis, which creates an asymmetric thermal gradient and defines the axes for the

resulting birefringence gradient. By aligning the laser polarization with the birefringence axes, the polarization gradient can be minimized. We have verified this both with polarimetry (23) and through the resulting ac Stark shift systematic (Fig. 3A).

Such ac Stark shift effects can cause a systematic shift in the measurement of $\omega^{N\mathcal{E}}$ in the presence of an $\tilde{N}\tilde{\mathcal{E}}$ -correlated detuning, $\Delta^{N\mathcal{E}}$, or Rabi frequency, $\Omega_r^{N\mathcal{E}}$. We observed both.

The detuning component $\Delta^{N\mathcal{E}}$ is caused by a nonreversing \mathcal{E} -field component, \mathcal{E}^{nr} , generated by patch potentials and technical voltage offsets, which is small relative to the reversing component, $|\mathcal{E}_z|\tilde{\mathcal{E}}$. The \mathcal{E}^{nr} creates an $\tilde{N}\tilde{\mathcal{E}}$ -correlated dc Stark shift with an associated detuning $\Delta^{N\mathcal{E}} = D\mathcal{E}^{nr}$, where D is the H state electric dipole moment. We measured \mathcal{E}^{nr} via microwave spectroscopy (Fig. 3B), two-photon Raman spectroscopy, and the $\tilde{N}\tilde{\mathcal{E}}$ -correlated contrast.

The Rabi frequency component, $\Omega_r^{N\mathcal{E}}$, arises from a dependence of Ω_r on the orientation of the molecular axis, $\hat{n} \approx \tilde{N}\tilde{\mathcal{E}}\hat{z}$, with respect to the laser propagation direction, \hat{k} . This $\hat{k} \cdot \hat{z}$ dependence can be caused by interference between E1 and M1 transition amplitudes on the $H \rightarrow C$ transition. Measurements of a nonzero $\tilde{N}\tilde{\mathcal{E}}$ -correlated fluorescence signal, $S^{N\mathcal{E}}$, and an $\tilde{N}\tilde{\mathcal{E}}\tilde{B}$ -correlated phase, $\phi^{N\mathcal{E}B}$ —both of which changed sign when we reversed \hat{k} —provided evidence for a nonzero $\Omega_r^{N\mathcal{E}}$. The $\phi^{N\mathcal{E}B}$ channel, along with its linear dependence on an artificial $\Omega_r^{N\mathcal{E}}$ generated by an $\tilde{N}\tilde{\mathcal{E}}$ -correlated laser intensity, allowed us to measure $\Omega_r^{N\mathcal{E}}/\Omega_r = (-8.0 \pm 0.8) \times 10^{-3}(\hat{k} \cdot \hat{z})$, where Ω_r is the uncorrelated (mean) Rabi frequency (see supplementary materials).

By intentionally exaggerating these parameters, we verified that both \mathcal{E}^{nr} and $\Omega_r^{N\mathcal{E}}$ couple to ac Stark shift effects to produce a false EDM. For the EDM data set, we tuned the laser polarization for each \tilde{G} state to minimize the magnitude of the systematic slope $\partial\omega^{N\mathcal{E}}/\partial\mathcal{E}^{nr}$ (Fig. 3A). The correlations $\partial\omega^{N\mathcal{E}}/\partial\mathcal{E}^{nr}$ and $\partial\omega^{N\mathcal{E}}/\partial\Omega_r^{N\mathcal{E}}$ were monitored at regular intervals throughout data collection (fig. S1E). The resulting systematic corrections to $\omega^{N\mathcal{E}}$ were all <1 mrad/s.

For a subset of our data, the \tilde{N} -correlated phase ϕ^N was nonzero and drifted with time. We identified the cause of this behavior as an \tilde{N} -correlated laser pointing $\hat{k}^N \cdot \hat{x} \approx 5 \mu\text{rad}$ present in our optical frequency switching setup. We eliminated this effect with improved optical alignment; however, we were not able to determine the precise mechanism by which \hat{k}^N coupled to ϕ^N , and so we chose to include ϕ^N variations in our systematic error budget. The slope $\partial\omega^{N\mathcal{E}}/\partial\phi^N$ (consistent with zero) and the mean value of ϕ^N established a systematic uncertainty limit of ~1 mrad/s on $\omega^{N\mathcal{E}}$.

To be cautious, we included in our systematic error budget possible contributions from the following parameters that caused a nonzero EDM shift in experiments similar to ours: stray B -fields $B_{x,y,z}^{nr}$ and B -field gradients (13); an $\tilde{\mathcal{E}}$ -correlated phase, $\phi^{\tilde{\mathcal{E}}}$, caused by leakage current, $\vec{v} \times \tilde{\mathcal{E}}$, and geometric phase effects (4); and laser detunings and

Fig. 3. The \mathcal{E}^{nr} systematic. (A) Tuning out laser polarization gradient and $\partial\omega^{N\mathcal{E}}/\partial\mathcal{E}^{nr}$ (see text for details). Red and black data points were taken with the polarization misaligned and aligned, respectively, with the birefringence axes of the electric field plates. Error bars represent 1σ statistical uncertainties. (B) Microwave spectroscopic measurement of \mathcal{E}^{nr} during normal operation along the molecule beam axis, x , with 1σ statistical error bars.

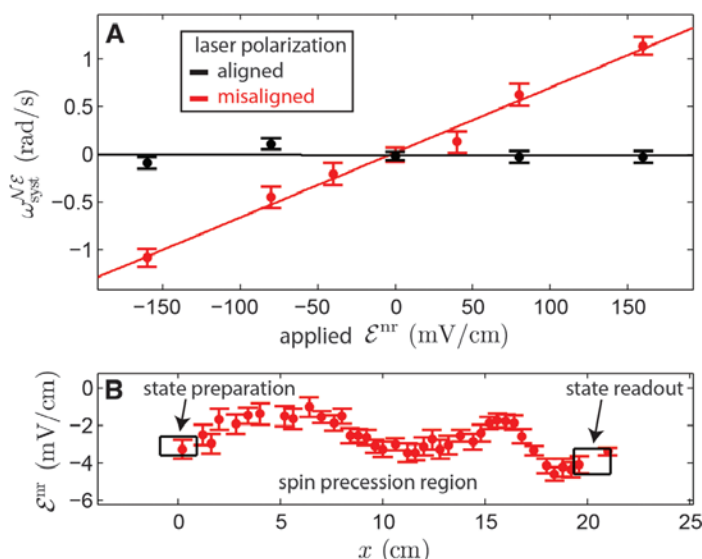


Table 1. Summary of systematic errors. Systematic and statistical errors for $\omega^{N\mathcal{E}}$, in units of mrad/s. All uncertainties are added in quadrature and are derived from Gaussian 1σ (68%) confidence intervals. In EDM units, $1.3 \text{ mrad/s} \approx 10^{-29} e \cdot \text{cm}$.

Parameter	Shift	Uncertainty
\mathcal{E}^{nr} correction	-0.81	0.66
$\Omega_r^{N\mathcal{E}}$ correction	-0.03	1.58
$\phi^{\tilde{\mathcal{E}}}$ -correlated effects	-0.01	0.01
ϕ^N correlation		1.25
Nonreversing B -field (B_z^{nr})		0.86
Transverse B -fields (B_x^{nr}, B_y^{nr})		0.85
B -field gradients		1.24
Prep./read laser detunings		1.31
\tilde{N} -correlated detuning		0.90
\mathcal{E} -field ground offset		0.16
Total systematic	-0.85	3.24
Statistical		4.80
Total uncertainty		5.79

\mathcal{E} -field ground offsets (5). We obtained direct $\omega^{N\mathcal{E}}$ systematic limits of ≤ 1 mrad/s for each. We simulated the effects that contribute to $\phi^{\mathcal{E}}$ by deliberately correlating \mathcal{B}_z with \mathcal{E} , which allowed us to place a $\sim 10^{-2}$ mrad/s limit on their combined effect. Because of our slow molecular beam, relatively small applied \mathcal{E} -fields, and small magnetic dipole moment, we do not expect any of these effects to systematically shift $\omega^{N\mathcal{E}}$ above the 10^{-3} mrad/s level (10, 11).

The result of this first-generation ThO measurement,

$$d_e = (-2.1 \pm 3.7_{\text{stat}} \pm 2.5_{\text{syst}}) \times 10^{-29} e\text{-cm} \quad (4)$$

comes from $d_e = -\hbar\omega^{N\mathcal{E}}/\mathcal{E}_{\text{eff}}$ using $\mathcal{E}_{\text{eff}} = 84$ GV/cm (8, 9) and $\omega^{N\mathcal{E}} = (2.6 \pm 4.8_{\text{stat}} \pm 3.2_{\text{syst}})$ mrad/s. This sets a 90% confidence limit,

$$|d_e| < 8.7 \times 10^{-29} e\text{-cm} \quad (5)$$

that is smaller than the previous best limit by a factor of 12 (4, 5)—an improvement made possible by the use of the ThO molecule and of a cryogenic source of cold molecules for this purpose. If we were to take into account the roughly estimated 15% uncertainty on the calculated \mathcal{E}_{eff} (8) and assume that this represents a 1σ Gaussian distribution width, the d_e limit stated above would increase by about 5%. Because paramagnetic molecules are sensitive to multiple time reversal (T)-violating effects (24), our measurement should be interpreted as $\hbar\omega^{N\mathcal{E}} = -d_e\mathcal{E}_{\text{eff}} - W_S C_S$, where C_S is a T-violating electron-nucleon coupling and W_S is a molecule-specific constant (8, 25). For the d_e limit above, we assume $C_S = 0$. Assuming instead that $d_e = 0$ yields $C_S = (-1.3 \pm 3.0) \times 10^{-9}$, corresponding to a 90% confidence limit $|C_S| < 5.9 \times 10^{-9}$ that is smaller than the previous limit by a factor of 9 (26).

A measurably large EDM requires new mechanisms for T violation, which is equivalent to combined charge-conjugation and parity (CP) violation, given the CPT invariance theorem (2). Nearly every extension to the Standard Model (27, 28) introduces new CP-violating phases ϕ_{CP} . It is difficult to construct mechanisms that systematically suppress ϕ_{CP} , so model builders typically assume $\sin(\phi_{\text{CP}}) \sim 1$ (29). An EDM arising from new particles at energy Λ in an n -loop Feynman diagram will have size

$$\frac{d_e}{e} \sim \kappa \left(\frac{\alpha_{\text{eff}}}{4\pi} \right)^n \left(\frac{m_e c^2}{\Lambda^2} \right) \sin(\phi_{\text{CP}}) (\hbar c) \quad (6)$$

where α_{eff} (about 4/137 for electroweak interactions) encodes the strength with which the electron couples to the new particles, m_e is the electron mass, and $\kappa \sim 0.1$ to 1 is a dimensionless prefactor (2, 30, 31). In models where 1- or 2-loop diagrams produce d_e , our result typically sets a bound on CP violation at energy scales $\Lambda \sim 3$ TeV or 1 TeV, respectively (27–29, 31). Hence, within the context of many models, our EDM limit constrains

CP violation up to energy scales similar to, or higher than, those explored directly at the Large Hadron Collider.

References and Notes

- P. G. H. Sandars, *Phys. Lett.* **14**, 194–196 (1965).
- I. B. Khriplovich, S. K. Lamoreaux, *CP Violation Without Strangeness* (Springer, New York, 1997).
- E. D. Commins, D. DeMille, in *Lepton Dipole Moments*, B. L. Roberts, W. J. Marciano, Eds. (World Scientific, Singapore, 2010), chap. 14, pp. 519–581.
- B. Regan, E. Commins, C. Schmidt, D. DeMille, *Phys. Rev. Lett.* **88**, 071805 (2002).
- J. J. Hudson *et al.*, *Nature* **473**, 493–496 (2011).
- D. M. Kara *et al.*, *New J. Phys.* **14**, 103051 (2012).
- M. A. Player, P. G. H. Sandars, *J. Phys. B* **3**, 1620–1635 (1970).
- L. V. Skripnikov, A. N. Petrov, A. V. Titov, *J. Chem. Phys.* **139**, 221103 (2013).
- E. R. Meyer, J. L. Bohn, *Phys. Rev. A* **78**, 010502 (2008).
- A. C. Vutha *et al.*, *J. Phys. B* **43**, 074007 (2010).
- A. C. Vutha *et al.*, *Phys. Rev. A* **84**, 034502 (2011).
- S. Bickman, P. Hamilton, Y. Jiang, D. DeMille, *Phys. Rev. A* **80**, 023418 (2009).
- S. Eckel, P. Hamilton, E. Kirilov, H. W. Smith, D. DeMille, *Phys. Rev. A* **87**, 052130 (2013).
- W. C. Campbell *et al.*, EPJ Web of Conferences **57**, 02004 (2013).
- E. Kirilov *et al.*, *Phys. Rev. A* **88**, 013844 (2013).
- S. E. Maxwell *et al.*, *Phys. Rev. Lett.* **95**, 173201 (2005).
- N. R. Hutzler *et al.*, *Phys. Chem. Chem. Phys.* **13**, 18976 (2011).
- N. R. Hutzler, H.-I. Lu, J. M. Doyle, *Chem. Rev.* **112**, 4803–4827 (2012).
- H. R. Gray, R. M. Whitley, C. R. Stroud Jr., *Opt. Lett.* **3**, 218–220 (1978).
- G. J. Feldman, R. D. Cousins, *Phys. Rev. D* **57**, 3873–3889 (1998).
- J. H. Curtiss, *Ann. Math. Stat.* **12**, 409–421 (1941).
- S. Eisenbach, H. Lotem, *Proc. SPIE* **1972**, 19 (1993).
- H. G. Berry, G. Gabrielse, A. E. Livingston, *Appl. Opt.* **16**, 3200–3205 (1977).
- M. G. Kozlov, L. N. Labzowsky, *J. Phys. At. Mol. Opt. Phys.* **28**, 1933–1961 (1995).
- V. A. Dzuba, V. V. Flambaum, C. Harabati, *Phys. Rev. A* **84**, 052108 (2011).
- W. C. Griffith *et al.*, *Phys. Rev. Lett.* **102**, 101601 (2009).
- S. Barr, *Int. J. Mod. Phys. A* **08**, 209–236 (1993).
- M. Pospelov, A. Ritz, *Ann. Phys.* **318**, 119–169 (2005).
- J. Engel, M. J. Ramsey-Musolf, U. van Kolck, *Prog. Part. Nucl. Phys.* **71**, 21–74 (2013).
- N. Fortson, P. Sandars, S. Barr, *Phys. Today* **56**, 33 (2003).
- W. Bernreuther, M. Suzuki, *Rev. Mod. Phys.* **63**, 313–340 (1991).

Acknowledgments: Supported by NSF and the Precision Measurement Grants Program of the National Institute of Standards and Technology. We thank M. Reece and M. Schwartz for discussions and S. Cotreau, J. MacArthur, and S. Sansone for technical support. P.W.H. was supported in part by the Office of Science Graduate Fellowship Program, U.S. Department of Energy. The authors declare no competing financial interests.

Supplementary Materials

www.sciencemag.org/content/343/6168/269/suppl/DC1

Materials and Methods

Fig. S1

Table S1

References (32–36)

7 November 2013; accepted 9 December 2013

Published online 19 December 2013;

10.1126/science.1248213

Single-Crystal Linear Polymers Through Visible Light-Triggered Topochemical Quantitative Polymerization

Letian Dou,^{1,2,3} Yonghao Zheng,^{1,4} Xiaoqin Shen,¹ Guang Wu,⁵ Kirk Fields,⁶ Wan-Ching Hsu,^{2,3} Huanping Zhou,^{2,3} Yang Yang,^{2,3}† Fred Wudl^{1,4,5,*}†

One of the challenges in polymer science has been to prepare large-polymer single crystals. We demonstrate a visible light-triggered quantitative topochemical polymerization reaction based on a conjugated dye molecule. Macroscopic-size, high-quality polymer single crystals are obtained. Polymerization is not limited to single crystals, but can also be achieved in highly concentrated solution or semicrystalline thin films. In addition, we show that the polymer decomposes to monomer upon thermolysis, which indicates that the polymerization-depolymerization process is reversible. The physical properties of the polymer crystals enable us to isolate single-polymer strands via mechanical exfoliation, which makes it possible to study individual, long polymer chains.

Obtaining single-crystalline materials is of importance in chemistry, physics, and materials science because it enables not only a fundamental understanding of the nature of the materials through structure-function correlations but also provides a wide range of advanced applications (1–3). Different from inorganic compounds or organic small molecules, polymers tend to form amorphous or semicrystalline phases because of entanglements of the long and flexible backbone (4, 5). Preparing large-size polymer single crystals remains a challenge in polymer

science (6–8). Topochemical polymerization, a process whereby the confinement and preorganization of the solid state forces a chemical reaction to proceed with a minimum amount of atomic and molecular movement, has provided a promising solution (9, 10). Hasegawa *et al.* reported topochemical polymerization reactions of diolefin-related compounds (11, 12) and Wegner discovered the polymerization of the 1,4-disubstituted-1,3-diacetylene single crystals by heating or high-energy photon irradiation (13). It was found that, if the reactive monomers are